ACS APPLIED MATERIALS & INTERFACES

Research Article

www.acsami.org

Development of the Morphology during Functional Stack Build-up of P3HT:PCBM Bulk Heterojunction Solar Cells with Inverted Geometry

Weijia Wang,[†] Stephan Pröller,[†,‡] Martin A. Niedermeier,[†] Volker Körstgens,[†] Martine Philipp,[†] Bo Su,[†] Daniel Moseguí González,[†] Shun Yu,[§,∥] Stephan V. Roth,[§] and Peter Müller-Buschbaum*[,†]

[†]Technische Universität München, Physik-Department, Lehrstuhl für Funktionelle Materialien, James-Franck-Straße 1, 85748 Garching, Germany

[‡]Technische Universität München, Munich School of Engineering, Herzig Group, Lichtenbergstr. 4, 85748 Garching, Germany

[§]Deutsches Elektronen-Synchrotron (DESY), Notkestraße 85, 22603 Hamburg, Germany

[∥]KTH Royal Institute of Technology, School of Chemical Science and Engineering, Polymeric Materials & Wallenberg Wood Science Center (WWSC), Teknikringen 56-58, SE-100 44 Stockholm, Sweden

ABSTRACT: Highly efficient poly(3-hexylthiophene-2,5-diyl) (P3HT):phenyl-C61-butyric acid methyl ester (PCBM) bulk heterojunction solar cells are achieved by using an inverted geometry. The development of the morphology is investigated as a function of the multilayer stack assembling during the inverted solar cell preparation. Atomic force microscopy is used to reveal the surface morphology of each stack, and the inner structure is probed with grazing incidence small-angle X-ray scattering. It is found that the smallest domain size of P3HT is introduced by replicating the fluorine-doped tin oxide structure underneath. The structure sizes of the P3HT:PCBM active layer are further optimized after thermal annealing. Compared to devices with standard geometry, the P3HT:PCBM layer in the inverted solar cells shows smaller domain sizes, which are much closer to the exciton diffusion length in the polymer. The decrease in domain sizes is identified as the main reason for the improvement of the device performance.

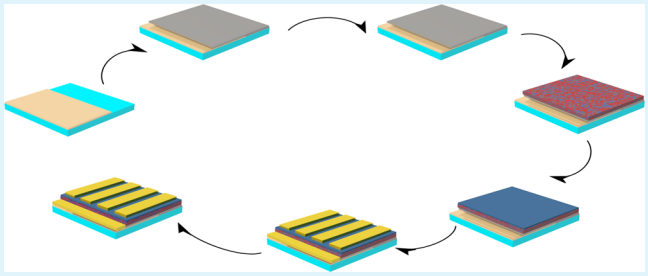

KEYWORDS: *P3HT:PCBM, BHJ solar cell, inverted solar cell, GISAXS, morphology*

1. INTRODUCTION

Organic photovoltaics, especially bulk heterojunction (BHJ) devices, are under intensive investigation since they present a promising route towards cost-efficient solar power conversion.[1−8] The main advantages of organic photovoltaics are related to their low weight and potential mechanical flexibility, low manufacturing costs and easy integration into other products, short times for the energy pay-off, and low environmental impact.[9−14] Further applications have been made to focus on organic solar cells, thus the efficiency has been improved continuously in the last decades.[10] It is noteworthy that the power conversion efficiency (PCE) of BHJ organic solar cells has already achieved efficiency values above 10% in champion cells by utilizing novel low band gap polymers.[15−17] Such PCE values start to become comparable to commercial silicon-based solar cells, and thus the possibility for industrialization and commercialization comes one more step closer.[18]

Today, poly(3-hexylthiophene-2,5-diyl) (P3HT):phenyl-C61-butyric acid methyl ester (PCBM) is the typical and most investigated combination of donor and acceptor materials for organic BHJ solar cells and thus can be regarded as a sort of model system for organic solar cells, although the reported PCE values do not reach up to those values achievable with low band gap polymers. From a morphology perspective, P3HT is a relatively unusual donor material since it tends to form fibrils much more readily than most conjugated polymers.[19] Generally, an improvement of the device performance can be achieved by optimization of the bicontinuous interpenetrating network between the donor and acceptor phases.[20] Many ways have been selected to optimize the morphology of BHJ films, such as thermal annealing, solvent vapor annealing, and solvent additive processing.[21−24] Alternatively, the inverted geometry is also introduced by several groups to increase the PCE of solar cells.[18,25−27] Xu et al. revealed that the inverted device (indium tin oxide (ITO)/cesium carbonate (Cs_2CO_3)/P3HT:PCBM/vanadium(V) oxide (V_2O_5)/aluminum (Al)) shows improved performance due to vertical phase separation in the P3HT:PCBM active layer.[28] Hsieh et al. further increased the PCE of the inverted solar cell (ITO/zinc oxide (ZnO)/P3HT:PCBM/poly(3,4-ethylenedioxy thiophene):poly(styrenesulfonate) (PEDOT:PSS)/silver (Ag)) from 3.5% to 4.4% by integrating a cross-linked fullerene material as an interlayer.[29] Although significant progress has been made by

Received: October 1, 2014
Accepted: December 11, 2014
Published: December 11, 2014

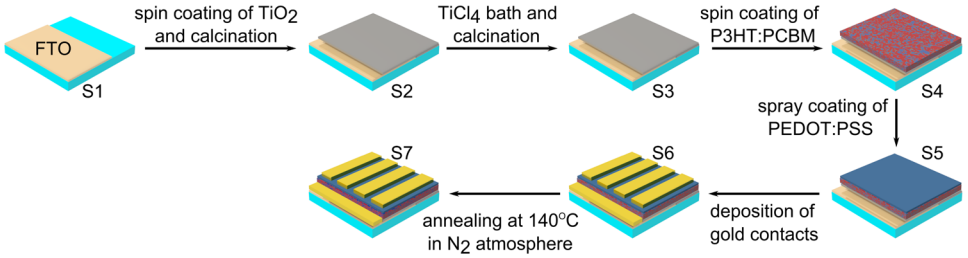

Figure 1. Scheme of the functional stacks on the basis of the preparation route of P3HT:PCBM solar cells with inverted geometry named after their preparation sequence S1 to S7.

using inverted geometry in solar cells, the fundamental understanding of the development of the morphologies during the complex functional stack assembling as well as the relationship between morphology and device performance are still missing. One reason is that most investigations are only focused on the active layer P3HT:PCBM and do not probe the full functional stack. Such investigations limited to the active layer do not account for the real architecture of the whole solar cell. However, the morphology evolution as a function of multilayer stack build-up needs investigation, especially for fundamental model systems such as the P3HT:PCBM active layer, to gain a deeper understanding. Grazing incidence small-angle X-ray scattering (GISAXS) is a powerful method to probe the inner morphology, including also the morphology of the active layer buried in between the electrodes. For example, Perlich et al. have already successfully employed GISAXS to investigate the tailored titania morphological evolution during the preparation route towards the functional multilayer stack of a dye-sensitized solar cell.[30] Recently, Guo et al. investigated the evolution of lateral structures during the functional stack build-up of P3HT:PCBM solar cells in standard geometry via GISAXS.[31]

In the present investigation we demonstrate that the PCE of the P3HT:PCBM BHJ solar cells can be significantly improved from 3.13 ± 0.1% (with standard geometry) to 4.23 ± 0.2% by introducing a simple inverted geometry to the solar cell architecture (FTO/TiO_2/P3HT:PCBM/PEDOT:PSS/Au). The maximum PCE value around 4.43% is among the highest values reported for P3HT:PCBM solar cells, especially using a titania hole blocking layer. The gradual development of the P3HT:PCBM BHJ morphology in an inverted solar cell is tracked by AFM and GISAXS measurements during functional stack build-up. More realistic information on each stack's morphology is provided compared to the nominal investigation exclusively limited to the P3HT:PCBM BHJ layer. Herein, the relationship between the high device performance and the inner morphologies of each functional stack is investigated and compared to the previously measured standard geometry.

2. EXPERIMENTAL SECTION

(a). Materials. The solvent chlorobenzene (Carl Roth) was used as supplied. Poly(3-hexylthiophene-2,5-diyl) (P3HT) was purchased from Rieke Metals, Inc. Its average molecular weight M_w was 50 000 g/mol, with a regioregularity of more than 95%. Phenyl-C61-butyric acid methyl ester (PCBM) was purchased from Nano-C with a purity of 99.5%. The used poly(3,4-ethylenedioxythiophene):poly-(styrenesulfonate) (PEDOT:PSS) solution, PH1000, with a PEDOT to PSS ratio of 1:2.5, was purchased from Ossila. Solar cells were fabricated on fluorine-doped tin oxide (FTO)/glass substrates purchased from Solaronix (size 2.2 × 2.2 cm^2).

(b). Sample Preparation. As the bottom electrode for the inverted solar cells, pattered FTO was used. FTO was partially removed from the glass substrate by chemical etching as depicted in Figure 1 (S1) and cleaned in four steps (in the order of alconox solution, ethanol, acetone, and isopropanol) in an ultrasonic bath. The cleaned FTO/glass substrates were treated with oxygen plasma for 10 min. The compact titania layer was prepared according to a route reported by Yu et al.[32] Before the P3HT:PCBM layer preparation, P3HT was first dissolved in chlorobenzene, then the P3HT solution was added to dissolved PCBM with a concentration of 24 mg/mL with a ratio of 1:1. The P3HT:PCBM solution was stirred overnight and then deposited via spin-coating on the titanium dioxide blocking layer. Diluted PEDOT:PSS was found to be a suitable electron blocking layer for spraying.[33] Therefore, 100 μL of filtered PEDOT:PSS solution diluted with 1000 μL of isopropanol was sprayed with a constant rate of 70 μL/s by a commercial airbrush gun on top of the prepared samples with 18 cm distance and then spin dried with 2000 rpm for 60 s. All the preparation steps described above were performed in air. To finalize the functional stack build-up gold electrodes were deposited by physical vapor deposition followed by thermal annealing at 140 °C for 10 min in a closed environment with a constant nitrogen flow. As a reference, a P3HT:PCBM BHJ solar cell with standard geometry was fabricated following the route described by Guo et al.[31] The active layer thicknesses of both types of solar cells were identical.

(c). Measurements. *Current–Voltage Characterization.* The current–voltage characteristics of the solar cells were probed under AM1.5 illumination and recorded by a source meter, Keithley 2400. Before the measurement, the solar simulator Solar Constant1200 (K.H. Steuernagel Lichttechnik GmbH) was calibrated to 1000 W/m^2 via a silicon-based reference solar cell (WPVS, CalLab-Fraunhofer ISE). The pixel size was defined with a shadow mask and measured using a calibrated microscope. According to previous measurements, the diffusion of gold into the polymer films as well as the nonvisible parts of the gold electrodes were extremely small compared to the pixel size and therefore negligible.[34] More than 30 solar cells were prepared and tested for each geometry.

External Quantum Efficiency (EQE) Characterization. The EQE measurements were performed in a "Quantum Efficiency/IPCE Measurement Kit" developed by Newport, Corporation (Irvine, CA, USA). The light source consisted of a Xenon lamp. The light was chopped at a frequency of 27 Hz and preliminarily filtered through an optical filter. Afterwards, the beam entered the monochromator (Cornerstone 260, 74125), and the desired wavelength impinged on the sample through the same shadow mask used in the current–voltage characterization. The electric signal yielded by the sample was collected, and the frequency provided by the chopper was filtered via a Lock-In Amplifier (Merlin, 70104) before it was sent to the computer. Afterwards, the signal was processed by the software TracQ Basic 6, also provided by Newport Corporation. The samples were measured in the region of the electromagnetic spectrum of high response for P3HT:PCBM (300–800 nm). The calibration of the EQE system was performed with a silicon reference diode (Newport, 70356).

Scanning Electron Microscopy (SEM). An N-Vision 40 SEM (Zeiss) was used to get the two-dimensional topography images. Measurements were performed with the acceleration voltage of 1.0 kV at a working distance of 2.0 mm. The inverted solar cell was broken

dx.doi.org/10.1021/am5067749 | ACS Appl. Mater. Interfaces 2015, 7, 602–610

straightly after treatment in liquid nitrogen for cross-sectional measurements.

Grazing Incidence Small-Angle X-ray Scattering (GISAXS). The GISAXS experiments were performed at the P03/MiNaXS beamline of the PETRA III storage ring at DESY, Hamburg, Germany.[35,36] The X-ray wavelength was 0.0957 nm. A constant incident angle of 0.45° was selected for all the samples, which was above the critical angles of the polymers, FTO and gold. At this incident angle, the sample was fully penetrated, and both surface and inner film structures were probed. The sample detector distance was chosen to be 3180 mm to get a suitable q range. In order to analyze the GISAXS data, selected line cuts of the two-dimensional GISAXS data were performed in horizontal and vertical direction (with respect to the sample surface). To analyze the horizontal line cut data, a model in the framework of the distorted wave Born approximation (DWBA) using the local monodisperse approximation (LMA) was applied. The model assumed contributions from form factors of individual scattering objects, together with corresponding structure factors. A one-dimensional paracrystalline arrangement of the scattering objects was assumed. To describe the data, three cylindrical form factors (average structure size), each with a Gaussian distribution, were assumed simultaneously. Moreover, a Gaussian distributed structure factor (average center-to-center distances between structures) was assigned to each form factor.

Atomic Force Microscopy (AFM). The surface morphology of all the samples was probed by an Autoprobe CP Research AFM instrument (Veeco Metrology Group) in non-contact mode. The operated cantilever had a resonance frequency around 60 kHz.

3. RESULTS AND DISCUSSION

Figure 1 displays the investigated functional stack build-up of a P3HT:PCBM solar cell with inverted geometry as well as the corresponding fabrication. Similar to P3HT:PCBM solar cells in standard geometry, functional multiple stacks are sandwiched between two different electrodes in inverted geometry. However, for the inverted geometry, indium tin oxide (ITO) is replaced by fluorine-doped tin oxide (FTO) as the cathode for the high-temperature stability of FTO. Gold is used as the anode on top to match the work function of the materials in the device. In between the electrodes, two blocking layers and the active layer of P3HT:PCBM are deposited. The hole blocking layer made of compact titanium dioxide is deposited on top of FTO/glass, underneath the active layer. It is treated with a titanium tetrachloride ($TiCl_4$) bath to get a finer layer structure. The PEDOT:PSS layer is spray-coated on top of the active layer as the electron blocking layer. After deposition of the gold contact on top of the PEDOT:PSS layer, thermal annealing is applied to the complete device as the final step in a controlled environment with constant nitrogen flow, leading to a higher ordered semicrystalline P3HT phase.[37,38]

In brief, the partly chemically etched and precleaned FTO substrate is named as S1. S2 and S3 denote the compact titanium dioxide layer with calcination before and after a $TiCl_4$ bath treatment, respectively. Sample S4 resulted from spin-coating P3HT:PCBM. It is followed by the deposition of a PEDOT:PSS layer denoted as S5. Gold evaporation and annealing are named as sample S6 and S7, respectively.

3.1. Solar Cell Performance. Figure 2a presents the $J-V$ curves of the P3HT:PCBM BHJ solar cells both, with standard geometry and inverted geometry in the dark and under solar illumination (AM1.5). The photovoltaic performance of the corresponding solar cells is characterized by the short circuit current (J_{SC}), open circuit voltage (V_{OC}), fill factor (FF), and power conversion efficiency (PCE), which are displayed in Table 1. It is notable that the inverted solar cells have a much higher value of J_{SC} (13.1 ± 0.3 mA/cm^2) as compared to the

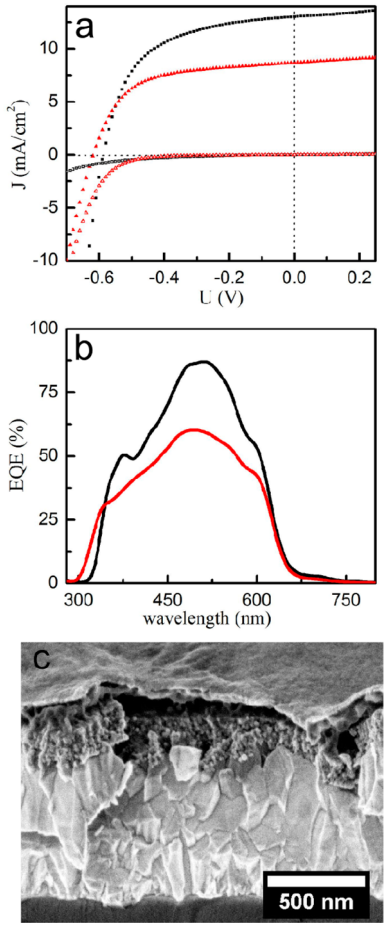

Figure 2. (a) $J-V$ curves of P3HT:PCBM BHJ solar cells with standard geometry (red triangles) and inverted geometry (black squares). Filled symbols are under illumination, and the open symbols are in dark condition. (b) EQE of P3HT:PCBM solar cell with standard geometry (red curve) and inverted geometry (black curve). (c) SEM cross-section image of the inverted P3HT:PCBM BHJ solar cell.

standard solar cells (8.9 ± 0.2 mA/cm^2). The values of V_{OC} of these two types of solar cells are in a similar range (0.62 ± 0.01 V for the standard solar cells and 0.58 ± 0.01 V for the inverted solar cells), due to the fact that the V_{OC} of the BHJ polymer–fullerene solar cell is determined mainly by the HOMO level of the donor and the LUMO level of the acceptor.[39] Furthermore, fill factors of the inverted solar cells achieve 55.9 ± 0.7%, which is almost the same as compared to the standard solar cells (FF = 57.4 ± 1.3%). The series resistance (R_s) and shunt resistance (R_{sh}) are also extracted from the $J-V$ curves and listed in Table 1. The relatively low R_s values in the inverted solar cells contribute to higher J_{SC}, as compared to the standard solar cells. However, the lower R_{SH} values in the inverted solar cells result in slightly lower values of V_{OC} and FF than these in standard solar cells. The lower R_{SH} values in inverted solar cells might be related to the less homogeneous and rougher PEDOT:PSS layer produced by spray-coating than that by spin-coating in standard geometry. In total, the PCE values of the inverted solar cells are improved from 3.13 ± 0.1% to 4.23 ± 0.2%, with a maximum value around 4.43%. The enhanced PCE values of the inverted solar cells originate from the improved J_{SC}. Furthermore, measured external quantum efficiency (EQE) curves in the range from 300 to 800 nm of both standard and

dx.doi.org/10.1021/am5067749 | ACS Appl. Mater. Interfaces 2015, 7, 602–610

Table 1. Comparison of Parameters of P3HT:PCBM Solar Cells with Standard and Inverted Geometry

geometry	J_{SC} (mA/cm^2)	U_{OC} (V)	FF (%)	PCE (%)	R_s (Ω cm^2)	R_{sh} (Ω cm^2)
standard	8.9 ± 0.2	−0.62 ± 0.01	57.4 ± 1.3	3.13 ± 0.1	12 ± 2	473 ± 42
inverted	13.1 ± 0.1	−0.58 ± 0.01	55.9 ± 0.7	4.23 ± 0.2	7 ± 1	340 ± 45

inverted solar cells are shown in Figure 2b. The typical shape of the EQE curve of P3HT:PCBM BHJ solar cells is present for both types of solar cells. The inverted solar cells show extremely high EQE values as compared to the standard solar cells. This difference in EQE between standard and inverted geometry is consistent with the J_{SC} values obtained from $J-V$ measurements. For comparison, Liu et al. also reached a quite high internal quantum efficiency of up to 0.9 electrons per photon in a P3HT:PCBM-based system, which is close to the maximum achievable, owing to reflections at the various interfaces and parasitic absorptions.[40]

A cross-section SEM image of the P3HT:PCBM solar cell with inverted geometry is depicted in Figure 2c. The FTO electrode (bright color) is localized at the bottom of the image showing a thickness of around 700 nm. On top of that the compact titanium dioxide layer (around 200 nm thick) is found. Polymer films of P3HT:PCBM and PEDOT:PSS are located above the compact titanium dioxide layer. Due to the low conductivity of these polymers compared to the other materials, they show a dark color and cannot be distinguished as two layers in the SEM image. The electrode including evaporated gold can be observed at the top of the image. Besides the stack geometry illustrated in Figure 2c, the good contact between layers is also observed, which is one of the basic premises for good photovoltaic performance of the inverted solar cell.

3.2. Structural Characterization. To observe the development of the surface morphology of P3HT:PCBM BHJ solar cells with inverted geometry during functional stack build-up, each step of assembling from S1 to S7 is investigated by atomic force microscopy (AFM) and shown in Figure 3. The surface structure of the bare FTO electrode (S1) is illustrated in Figure 3a, exhibiting a high roughness. After spin coating titanium dioxide (S2), a compact dot-like nanomorphology is observed, and then the denser nanomorphology is formed with $TiCl_4$ bath treatment (S3). However, the large height scale is still observed, which is attributed to the rough FTO substrate underneath. After further addition of the P3HT:PCBM layer its surface shows an interconnected nanomorphology (S4). However, the buried dot-like structure is still visible with slightly increased sizes, which is due to the replication of the titanium dioxide. After spray-coating the PEDOT:PSS layer (S5) on top, the surface morphology shows similar features but with slightly coarser structures. After evaporation of the gold contacts (S6 and S7), the gold layer shows a different surface morphology than the PEDOT:PSS layer underneath. The grain-shaped morphology is attributed to the clusters of small gold particles.

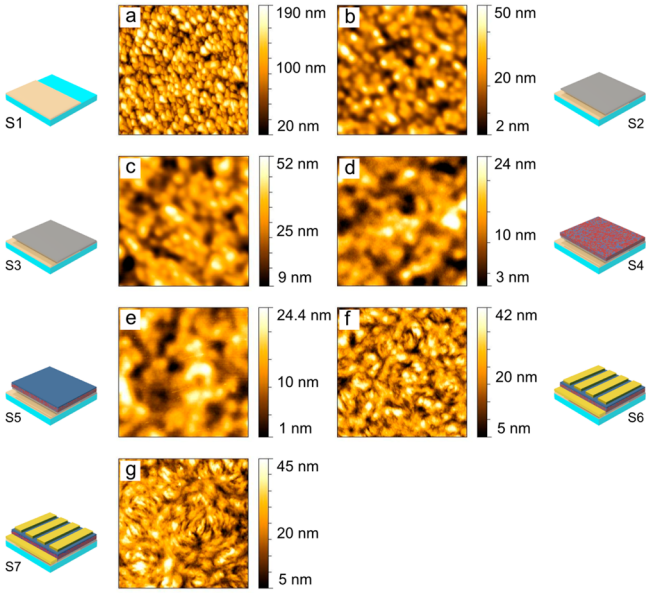

Figure 3. AFM topography images (4 × 4 μm^2) of the functional stacks from S1 to S7, labeled as (a) to (g) as indicated by the icons. The height scale bar is adapted individually to account for the different roughness of the surfaces.

The surface roughness is extracted from the AFM topography measurements and plotted in Figure 4. The surface roughness of the FTO-coated substrate is about 29 nm, which is much larger than the surface roughness of the ITO electrodes used in standard solar cells. This rougher surface structure of FTO may increase the internal light scattering and accordingly improve the light harvesting efficiency. This could be one reason for the increased J_{SC} and accordingly higher PCE values of the inverted solar cells. It was reported in the work done by Kim et al. that enhancement of light harvesting has been achieved by using structured substrates.[41] Meier et al. achieved an increase of the PCE by introducing a grating-type pattern into the functional stack of a P3HT:PCBM BHJ solar cell.[42] In our functional stack build-up the sample surface is flattened with the addition of the titanium dioxide layer (S2). The surface roughness is further decreased after the $TiCl_4$ bath treatment (S3). The roughness of the P3HT:PCBM surface is found to be around 5 nm, which is a larger value as compared to the ones reported in investigations addressing only the active layer deposited on a "flat" substrate. For example, a P3HT:PCBM film spin-coated on top of a silicon substrate was shown to exhibit a surface roughness of about 1 nm.[37] Thus, the roughness of the P3HT:PCBM film in the stack build-up (S4) in the inverted solar cells is larger due to the replication of the rough FTO surface underneath. This

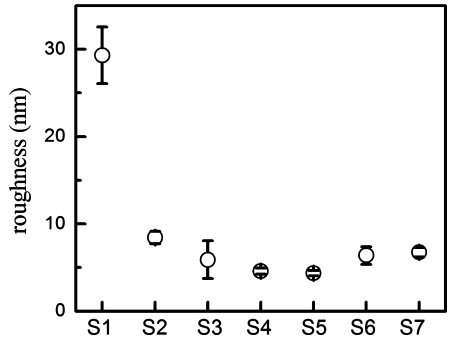

Figure 4. Surface roughness of functional stacks from S1 to S7 extracted from AFM measurements.

dx.doi.org/10.1021/am5067749 | ACS Appl. Mater. Interfaces 2015, 7, 602−610

increased roughness of the active layer could be beneficial for reducing the light reflection and accordingly contribute to higher J_{SC} of the solar cell with this inverted geometry. The spray-coated PEDOT:PSS layer (S5) has a surface roughness similar to the active layer, which demonstrates that no dewetting had occurred as was observed in the case of spin coating the PEDOT:PSS layer on top of P3HT:PCBM. For the functional stacks with deposited gold contacts (S6 and S7), the roughness is slightly increased again due to the growth mechanism of the evaporated gold on the polymer surface.[43,44]

Although AFM topography measurements reveal the surface morphology of the functional stack build-up in inverted solar cells, the obtained structural information at the surface can differ from the one inside the layers.[37] As known, the inner morphology, especially the phase separation of the BHJ active layer, is crucial for gaining a complete understanding of the solar cell. To address the inner structure, grazing incidence small-angle X-ray scattering (GISAXS) is applied. With this technique, mesoscopic structures can be characterized.[45−49] GISAXS has been proven to be very powerful in analyzing materials for application in organic photovoltaics.[21,50−56] Therefore, GISAXS measurements of all functional stacks are carried out to track the progress of the morphology in our system.

In Figure 5 the two-dimensional (2D) GISAXS data of each step of the functional stack build-up of the P3HT:PCBM

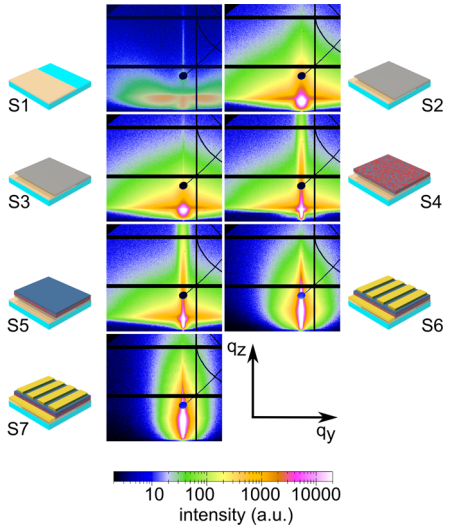

Figure 5. 2D GISAXS data of the functional stacks from samples S1 to S7 as indicated by the icons. The intensity scale bar is taken identical for all samples to illustrate the changes in scattered intensity.

inverted solar cell are shown. For all the measurements, the specularly reflected beam (specular peak) in the center of the scattering pattern is shielded by a point-shaped beamstop to avoid the oversaturation of the detector. The material-specific Yoneda peak, located at the position of the critical angle (FTO 0.223°, TiO_2 0.173°, P3HT 0.105°, PEDOT:PSS 0.092°, and gold 0.343°), is clearly visible as a bright region underneath the beamstop. The FTO substrate (S1) shows a clear wing-like feature in horizontal direction, which indicates that the FTO has structure sizes in the lower nanometer length scale. After adding the titanium dioxide layers (S2 and S3), the 2D GISAXS scattering patterns change considerably. In addition, the scattering intensity increases evidently. This increased scattering intensity is attributed to the flattened surface after deposition of the titanium dioxide, which is consistent with the AFM surface roughness investigation. Continuing with spin coating the P3HT:PCBM blend on top, the Yoneda region is altered pronouncedly due to the addition of new materials with other scattering length densities. After the PEDOT:PSS layer (S5) deposition a similar 2D GISAXS pattern is observed, which is probably induced by low scattering contrast between these polymers. The scattering patterns of the stacks with gold contact (S6 and S7) completely differ from those of the previous functional stacks. This pronounced change is caused by the higher scattering intensity from the top layer of gold in comparison to that of the other materials. Additionally, a narrowed scattering pattern is observed after thermal annealing, which suggests an increase in lateral structure size.

To get information on the structure along the surface normal of the films vertical line cuts are extracted from the 2D GISAXS data. The vertical cuts are taken at the position $q_y = 0$ and presented in Figure 6 for each step of the functional stack build-

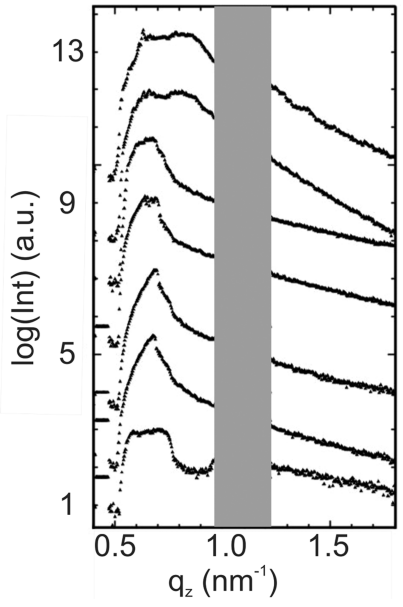

Figure 6. Vertical line cuts of the 2D GISAXS data measured at the functional stacks (S1 to S7 shown from bottom to top). The position of the beam stop is indicated by the gray rectangle. The curves are shifted along the intensity axis for clarity of the presentation.

up (S1 to S7 from bottom to top). The dented intensity, caused by shielding the specular peak with the beamstop, is indicated by the gray bar in the figure. For all curves, the intensity is dominated by the Yoneda peaks at low q_z values (around 0.5−0.9 nm^{-1}). As the Yoneda peak position is material sensitive, after addition of the next layers containing new materials to the functional stack, additional Yoneda peaks become visible.[57] For example, after spin coating the P3HT:PCBM film, new Yoneda peaks appear in the vertical line cut, which are due to the presence of P3HT:PCBM. The Yoneda peaks corresponding to both FTO and titanium dioxide are still visible. However, for this functional stack the FTO Yoneda peak is not as pronounced, since it is superimposed by the Yoneda peaks of titanium dioxide and P3HT:PCBM. Throughout all the vertical line cuts, the feature of each material is resolved as shown in the Yoneda region. Therefore, it is inferred that there are no

dx.doi.org/10.1021/am5067749 | ACS Appl. Mater. Interfaces 2015, 7, 602−610

changes of the specific material properties during the solar cell device assembling process.

Similarly to the investigation of structures vertical to the film plane, lateral structure information can also be obtained by applying horizontal line cuts to the 2D GISAXS data. The horizontal line cut performed at the Yoneda peak position of a particular material shows the most pronounced scattering intensity of this material.[49] Thus, for functional stacks from S1 to S3, the horizontal line cuts are performed at the Yoneda peak positions of the layer material newly deposited, such as at the FTO position for sample S1 and at the titanium dioxide position for samples S2 and S3. Due to the fact that the nanomorphology of P3HT:PCBM strongly influences the photovoltaic performance of the solar cells, the understanding of the evolution of the P3HT:PCBM morphology is most interesting for all steps of the solar cell build-up. Thus, after deposition of the active layer the horizontal line cuts are performed at the Yoneda peak position of P3HT (from S4 to S7). In Figure 7 the horizontal line cuts are arranged in the order of the build-up steps of the inverted solar cell (from bottom to top: S1 to S7). To obtain quantitative information, the horizontal line cuts are fitted with a model explained in the Experimental Section. It is taking the form factor (structure size, defined as the radius of the domain in this work) and structure factor (center-to-center distance) as well as the resolution into account.[49] The best obtained fits are also shown in Figure 7 as solid red lines.

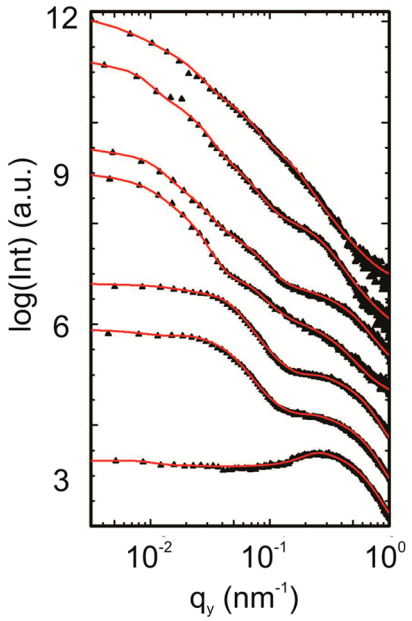

Figure 7. Horizontal line cuts of the 2D GISAXS data (dots) shown together with the best corresponding fits (solid red lines) of the functional stacks (S1 to S7 from bottom to top). The curves are shifted along the intensity axis for clarity of the presentation.

In the horizontal line cut of the GISAXS data measured at the FTO substrate (S1) one pronounced peak is observed as shown in Figure 7, which is correlated to a specific lateral FTO structure.[58] As compared to the horizontal line cut of ITO used in standard solar cells, which shows a broadly distributed shoulder,[31] the FTO substrate exhibits much better defined structure sizes. After deposition of the titanium dioxide layer (S2), the FTO peak is preserved, and a new peak appears at small q_y values. The $TiCl_4$ bath and the calcination (S3) do not alter the inner structure significantly. Continuing with spin coating the active layer P3HT:PCBM (S4) results in an obvious change. A new peak appears at smaller q_y values, which is indicating that large structures are formed, originating from P3HT:PCBM. Moreover, the structure size originating from FTO is reproduced by the active layer but less pronounced. After spray coating the PEDOT:PSS layer (S5) no strong changes of the inner film structure of the active layer occur since this is a low-temperature processing step. After evaporation of the gold top electrode (S6), the peak is shifted to a smaller q_y value, suggesting an increased structure size of P3HT. The peak is further shifted towards a smaller q_y value and broadly distributed when the sample is thermally annealed (S7).

In Figure 8 the structure sizes and distances extracted from the modeling of the horizontal line cuts are summarized.

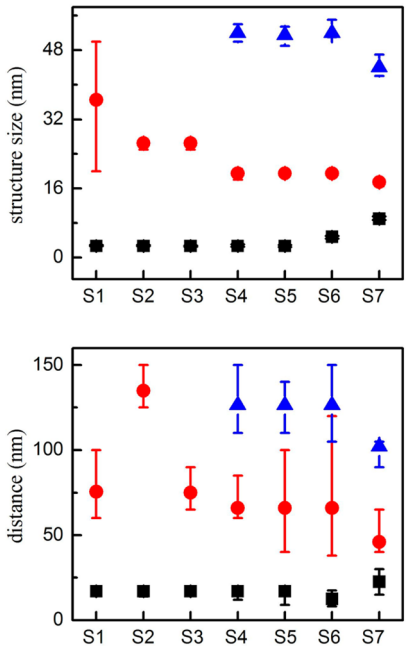

Figure 8. Characteristic structure sizes and distances as extracted from the modeling of horizontal line cuts. For FTO (S1) and titanium dioxide (S2, S3) two structure sizes are identified (small in black, large in red color), whereas for P3HT (S4 to S7) three structure sizes are found (small in black, medium size in red, and large in blue color).

According to the position of the cuts performed, the dominant structure information is assigned to FTO (S1), titanium dioxide (S2 and S3), and P3HT (from S4 to S7).

For FTO two characteristic sizes (2.7 and 36.5 nm structure sizes and corresponding 17 and 75.5 nm distances) are modeled to describe the data. After adding the titanium dioxide layers, the small FTO structure of 2.7 nm is replicated by titanium dioxide (S2 and S3). Moreover, a new structure size of 26.5 nm with a center-to-center distance of 135 nm is observed (S2), which is attributed to the presence of titanium dioxide nanoparticles. After the $TiCl_4$ bath treatment (S3), the structure size of these titanium dioxide nanoparticles (26.5 nm) remains unchanged, whereas their distance is decreased, which is consistent with the observations from AFM measurements. This decreased distance may be due to the gaps between the

dx.doi.org/10.1021/am5067749 | ACS Appl. Mater. Interfaces 2015, 7, 602−610

titanium particles filled during the $TiCl_4$ bath treatment, which implies that a finer layer of titanium dioxide is formed.

Depositing the P3HT:PCBM layer (S4) further replicates the small FTO structure (2.7 nm structure size and 17 nm distance). Furthermore, the appearance of two new structures belonging to P3HT, with structure sizes of 19.5 and 52 nm and corresponding distances of 66 and 126.5 nm, can be observed. After spray coating the PEDOT:PSS layer (S5), there are still three structures inside the active layer obtained, and no changes in the structure sizes and distances are present, which indicates that with addition of the PEDOT:PSS layer the morphology of the P3HT:PCBM layer is preserved.

A coarsened structure size of P3HT around 4.8 nm is observed after gold deposition (S6), which is probably caused by the thermal load applied during the evaporation of gold. The same trend was found in a standard solar cell, for which an increased structure size of P3HT was also observed after aluminum deposition on as-prepared P3HT:PCBM films.[31] However, the other two structures belonging to P3HT are preserved after gold deposition. Directly after gold deposition, the solar cell is annealed at 140 °C in a controlled environment with constant nitrogen flow (S7). The most interesting observation is that the smallest structure of P3HT is further increased from 4.8 nm to about 9 nm. Such coarsening of P3HT structures was also observed after thermal annealing in other studies.[2,31] In general, the P3HT crystallization via thermal annealing contributes to the coarsened structures, which is also a benefit for the charge transport in the respective materials. Accordingly, less interfaces between P3HT and PCBM phases are formed, which lowers the recombination probability. The P3HT objects with 9 nm structure size contribute to the efficient exciton dissociation since this length scale matches well with the exciton diffusion length of 10 nm reported for the polymer P3HT.[53] In addition, after thermal annealing, the other two structures of P3HT both decrease from 19.5 to 17.5 nm and 52 to 44 nm, which suggests the exciton dissociation is further improved due to smaller P3HT domains and therefore an easier diffusion of excitons to the interface. Compared to the solar cell with standard geometry, in which the P3HT:PCBM film after thermal annealing exhibits a much larger structure size of around 65 nm,[31] the smaller structure size in the inverted solar cell is definitively more beneficial. Therefore, the much higher J_{SC} and PCE of the solar cells with inverted geometry compared to the standard geometry must be explained by the smaller structure sizes in the P3HT:PCBM active layer.

4. CONCLUSIONS

In this work, we demonstrate a highly efficient polymer solar cell based on the P3HT:PCBM BHJ system in an inverted geometry. The PCE of the inverted solar cell is improved to 4.23 ± 0.2%, with a maximum value around 4.43%, as compared to the standard solar cell with PCE of 3.13 ± 0.1%. This is among the highest values reported for P3HT:PCBM solar cells. Moreover, it is notable that the inverted P3HT:PCBM solar cell owns much higher J_{SC} (13.1 ± 0.3 mA/cm^2) as compared to the standard solar cell (8.9 ± 0.2 mA/cm^2), which is considered as the main factor for the high efficiency.

To better understand the relationship between the improved device performance and the morphology of the inverted solar cells, AFM and GISAXS measurements are performed on each step of the multilayer stack build-up during the solar cell assembling. First of all, a high roughness of the FTO substrate is revealed by AFM measurements, which could increase the internal light scattering and accordingly improve the light harvesting efficiency. Additionally, through successfully employing GISAXS, there are three prominent structures observed for the P3HT:PCBM stack on the titanium dioxide blocking layer (S4) with structure sizes of 2.7, 19.2, and 52 nm. The smallest structure of 2.7 nm is attributed to the replication of the FTO substrate underneath. After final thermal annealing, the smallest P3HT structure size increases to 9 nm, which is in good agreement with the exciton diffusion length in the polymer. Moreover, the other two large structures reduce to 17.5 and 44 nm, which is smaller than the sizes found for the standard solar cells. These two smaller structure sizes are much closer to the exciton diffusion length in the polymer P3HT for the inverted as compared with the standard geometry and correspondingly lead to higher exciton dissociation efficiency. It is concluded that the high performance of the inverted P3HT:PCBM BHJ solar cells is due to the high roughness of the FTO substrate and the small domain sizes in the P3HT:PCBM active layer. Thus, our investigation shows that proper tuning of the bottom electrode surface structures can be interesting for improved device efficiencies.

AUTHOR INFORMATION

Corresponding Author

*E-mail: muellerb@ph.tum.de.

Notes

The authors declare no competing financial interest.

ACKNOWLEDGMENTS

Financial support by TUM.solar in the frame of the Bavarian Collaborative Research Project "Solar technologies go Hybrid" (SolTec), by the GreenTech Initiative (Interface Science for Photovoltaics - ISPV) of the EuroTech Universities and by the Nanosystems Initiative Munich (NIM) is acknowledged. V.K. thanks the Bavarian State Ministry of Sciences, Research and Arts for funding this research work via project "Energy Valley Bavaria". W.W. and B.S. acknowledge the China Scholarship Council (CSC). The authors thank D. Magerl for implementing the fitting model for horizontal line cuts of 2D GISAXS data. Portions of this research were carried out at the synchrotron light source PETRA III at DESY. DESY is a member of the Helmholtz Association (HGF).

REFERENCES

(1) Yu, G.; Gao, J.; Hummelen, J. C.; Wudl, F.; Heeger, A. J. Polymer Photovoltaic Cells: Enhanced Efficiencies via a Network of Internal Donor-Acceptor Heterojunctions. *Science* **1995**, *270*, 1789−1791.

(2) Li, G.; Shrotriya, V.; Yao, Y.; Yang, Y. Investigation of Annealing Effects and Film Thickness Dependence of Polymer Solar Cells Based on Poly(3-hexylthiophene). *J. Appl. Phys.* **2005**, *98*, 043704.

(3) Ma, W.; Yang, C.; Gong, X.; Lee, K.; Heeger, A. J. Thermally Stable, Efficient Polymer Solar Cells with Nanoscale Control of the Interpenetrating Network Morphology. *Adv. Funct. Mater.* **2005**, *10*, 1617−1622.

(4) Peet, J.; Kim, J. Y.; Coates, N. E.; Ma, W. L.; Moses, D.; Heeger, A. J.; Bazan, G. C. Efficiency Enhancement in Low-bandgap Polymer Solar Cells by Processing with Alkane Dithiols. *Nat. Mater.* **2007**, *6*, 497−500.

(5) Graetzel, M.; Janssen, R. A. J.; Mitzi, D. B.; Sargent, E. H. Materials Interface Engineering for Solution-processed Photovoltaics. *Nature* **2012**, *488*, 304−312.

(6) Menke, S. M.; Luhman, W. A.; Holmes, R. J. Tailored Exciton Diffusion in Organic Photovoltaic cells for Enhanced Power Conversion Efficiency. *Nat. Mater.* **2013**, *12*, 152−157.
(7) Zhou, H.; Zhang, Y.; Seifter, J.; Collins, S. D.; Luo, C.; Bazan, G. C.; Nguyen, T.-Q.; Heeger, A. J. High-Efficiency Polymer Solar Cells Enhanced by Solvent Treatment. *Adv. Mater.* **2013**, *25*, 1646−1652.
(8) Tumbleston, J. R.; Collins, B. A.; Yang, L.; Stuart, A. C.; Gann, E.; Ma, W.; You, W.; Ade, H. The Influence of Molecular Orientation on Organic Bulk Heterojunction Solar Cells. *Nat. Photonics* **2011**, *7*, 5482−5493.
(9) Ruderer, M. A.; Müller-Buschbaum, P. Morphology of Polymer-based Bulk Heterojunction Films for Organic Photovoltaics. *Soft Matter* **2014**, *8*, 385−391.
(10) Scharber, M. C.; Sariciftci, N. S. Efficiency of Bulk-heterojunction Organic Solar Cells. *Prog. Polym. Sci.* **2013**, *38*, 1929−1940.
(11) Brabec, C. J.; Sariciftci, N. S.; Hummelen, J. C. Plastic Solar Cells. *Adv. Funct. Mater.* **2001**, *11*, 15−26.
(12) Kaltenbrunner, M.; White, M. S.; Głowacki, E. D.; Sekitani, T.; Someya, T.; Sariciftci, N. S.; Bauer, S. Ultrathin and Lightweight Organic Solar Cells with High Flexibility. *Nat. Commun.* **2012**, *3*, 770.
(13) Burke, D. J.; Lipomi, D. J. Green Chemistry for Organic Solar Cells. *Energy Environ. Sci.* **2013**, *6*, 2053−2066.
(14) Darling, S. B.; You, F. The Case for Organic Photovoltaics. *RSC Adv.* **2013**, *3*, 17633−17648.
(15) You, J.; Dou, L.; Yoshimura, K.; Kato, T.; Ohya, K.; Moriarty, T.; Emery, K.; Chen, C.-C.; Gao, J.; Li, G.; Yang, Y. A Polymer Tandem Solar Cell with 10.6% Power Conversion Efficiency. *Nat. Commun.* **2013**, *4*, 1446.
(16) Chen, C.-C.; Chang, W.-H.; Yoshimura, K.; Ohya, K.; You, J.; Gao, J.; Hong, Z.; Yang, Y. An Efficient Triple-Junction Polymer Solar Cell Having a Power Conversion Efficiency Exceeding 11%. *Adv. Mater.* **2014**, *26*, 5670−5677.
(17) Søndergaard, R.; Hösel, M.; Angmo, D.; Larsen-Olsen, T. T.; Krebs, F. C. Roll-to-roll Fabrication of Polymer Solar Cells. *Mater. Today* **2012**, *15*, 36−49.
(18) He, Z.; Zhong, C.; Su, S.; Xu, M.; Wu, H.; Cao, Y. Enhanced Power-conversion Efficiency in Polymer Solar Cells Using an Inverted Device Structure. *Nat. Photonics* **2012**, *6*, 591−595.
(19) Chen, W.; Nikiforov, M. P.; Darling, S. B. Morphology Characterization in Organic and Hybrid Solar Cells. *Energy Environ. Sci.* **2012**, *5*, 8045−8074.
(20) Westacott, P.; Tumbleston, J. R.; Shoaee, S.; Fearn, S.; Bannock, J. H.; Gilchrist, J. B.; Heutz, S.; deMello, J.; Heeney, M.; Ade, H.; Durrant, J.; McPhail, D. S.; Stingelin, N. On the Role of Intermixed Phases in Organic Photovoltaic Blends. *Energy Environ. Sci.* **2013**, *6*, 2756−2764.
(21) Verploegen, E.; Mondal, R.; Bettinger, C. J.; Sok, S.; Toney, M. F.; Bao, Z. Effects of Thermal Annealing Upon the Morphology of Polymer−Fullerene Blends. *Adv. Funct. Mater.* **2010**, *20*, 3519−3529.
(22) Lou, S.; Szarko, J. M.; Xu, T.; Yu, L.; Marks, T.; Chen, L. X. Effects of Additives on the Morphology of Solution Phase Aggregates Formed by Active Layer Components of High-Efficiency Organic Solar Cells. *J. Am. Chem. Soc.* **2011**, *133*, 20661−20663.
(23) Chen, L.-M.; Hong, Z.; Li, G.; Yang, Y. Recent Progress in Polymer Solar Cells: Manipulation of Polymer:Fullerene Morphology and the Formation of Efficient Inverted Polymer Solar Cells. *Adv. Mater.* **2009**, *21*, 1434−1449.
(24) Liao, H.-C.; Ho, C.-C.; Chang, C.-Y.; Jao, M.-H.; Darling, S. B.; Su, W.-F. Additives for Morphology Control in High-Efficiency Organic Solar Cells. *Mater. Today* **2013**, *16*, 326−336.
(25) Li, G.; Chu, C.-W.; Shrotriya, V.; Huang, J.; Yang, Y. Efficient Inverted Polymer Solar Cells. *Appl. Phys. Lett.* **2006**, *88*, 253503.
(26) Glatthaar, M.; Niggemann, M.; Zimmermann, B.; Lewer, P.; Riede, M.; Hinsch, A.; Luther, J. Organic Solar Cells Using Inverted Layer Sequence. *Thin Solid Films* **2005**, *491*, 298−300.
(27) Ameri, T.; Dennler, G.; Waldauf, C.; Azimi, H.; Seemann, A.; Forberich, K.; Hauch, J.; Scharber, M.; Hingerl, K.; Brabec, C. J. Fabrication, Optical Modeling, and Color Characterization of Semitransparent Bulk-Heterojunction Organic Solar Cells in an Inverted Structure. *Adv. Funct. Mater.* **2010**, *20*, 1592−1598.
(28) Xu, Z.; Chen, L.-M.; Yang, G.; Huang, C.-H.; Hou, J.; Wu, Y.; Li, G.; Hsu, C.-S.; Yang, Y. Vertical Phase Separation in Poly(3-hexylthiophene): Fullerene Derivative Blends and its Advantage for Inverted Structure Solar Cells. *Adv. Funct. Mater.* **2009**, *19*, 1227−1234.
(29) Hsieh, C.-H.; Cheng, Y.-J.; Li, P.-J.; Chen, C.-H.; Dubosc, M.; Liang, R.-M.; Hsu, C.-S. Highly Efficient and Stable Inverted Polymer Solar Cells Integrated with a Cross-Linked Fullerene Material as an Interlayer. *J. Am. Chem. Soc.* **2010**, *132*, 4887−4893.
(30) Perlich, J.; Memesa, M.; Diethert, A.; Metwalli, E.; Wang, W.; Roth, S. V.; Timmann, A.; Gutmann, J. S.; Müller-Buschbaum, P. Preservation of the Morphology of a Self-encapsulated Thin Titania Film in a Functional Multilayer Stack: an X-ray Scattering Study. *ChemPhysChem* **2009**, *10*, 799−805.
(31) Guo, S.; Ruderer, M. A.; Rawolle, M.; Körstgens, V.; Birkenstock, C.; Perlich, J.; Müller-Buschbaum, P. Evolution of Lateral Structures during the Functional Stack Build-up of P3HT:PCBM-Based Bulk Heterojunction Solar Cells. *ACS Appl. Mater. Interfaces* **2013**, *5*, 8581−8590.
(32) Yu, H.; Zhang, S.; Zhao, H.; Will, G.; Liu, P. An Efficient and Low-cost TiO2 Compact Layer for Performance Improvement of Dye-sensitized Solar Cells. *Electrochim. Acta* **2009**, *54*, 1319−1324.
(33) Weickert, J.; Sun, H.; Palumbiny, C.; Hesse, H. C.; Schmidt-Mende, L. Spray-Deposited PEDOT:PSS for Inverted Organic Solar Cells. *Sol. Energy Mater. Sol. Cells* **2010**, *94*, 2371−2374.
(34) Ruderer, M. A.; Körstgens, V.; Metwalli, E.; Al-Hussein, M.; Vainio, U.; Roth, S. V.; Döhrmann, R.; Gehrke, R.; Gebhardt, R.; Burghammer, M.; Müller-Buschbaum, P. Determination of the Local Gold Contact Morphology on a Photoactive Polymer Film Using Nanobeam GISAXS. *Nucl. Instrum. Methods B* **2010**, *268*, 403−410.
(35) Buffet, A.; Rothkirch, A.; Döhrmann, R.; Körstgens, V.; Abul Kashem, M. M.; Perlich, J.; Herzog, G.; Schwartzkopf, M.; Gehrke, R.; Müller-Buschbaum, P.; Roth, S. V. P03, the Microfocus and Nanofocus X-ray Scattering (MiNaXS) Beamline of the PETRA III Storage Ring: the Microfocus Endstation. *J. Synchrotron Radiat.* **2012**, *19*, 647−653.
(36) Santoro, G.; Buffet, A.; Döhrmann, R.; Yu, S.; Körstgens, V.; Müller-Buschbaum, P.; Gedde, U.; Hedenqvist, M.; Roth, S. V. Use of Intermediate Focus for Grazing Incidence Small and Wide Angle X-ray Scattering Experiments at the Beamline P03 of PETRA III, DESY. *Rev. Sci. Instrum.* **2014**, *85*, 043901.
(37) Ruderer, M. A.; Guo, S.; Meier, R.; Chiang, H.-Y.; Körstgens, V.; Wiedersich, J.; Perlich, J.; Roth, S. V.; Müller-Buschbaum, P. Solvent-Induced Morphology in Polymer-Based Systems for Organic Photovoltaics. *Adv. Funct. Mater.* **2011**, *21*, 3382−3391.
(38) Yang, X.; Uddin, A. Effect of Thermal Annealing on P3HT:PCBM Bulk-Heterojunction Organic Solar Cells: A Critical Review. *Renewable Sustainable Energy Rev.* **2014**, *30*, 324−336.
(39) Scharber, M. C.; Mühlbacher, D.; Koppe, M.; Denk, P.; Waldauf, C.; Heeger, A. J.; Brabec, C. J. Design Rules for Donors in Bulk-Heterojunction Solar Cells—Towards 10% Energy-Conversion Efficiency. *Adv. Mater.* **2006**, *18*, 789−794.
(40) Liu, B.; Png, R.-Q.; Zhao, L.-H.; Chua, L.-L.; Friend, R. H.; Ho, P. K. H. High Internal Quantum Efficiency in Fullerene Solar Cells Based on Crosslinked Polymer Donor Networks. *Nat. Commun.* **2012**, *3*, 1321.
(41) Kim, J. B.; Kim, P.; Pégard, N. C.; Oh, S. J.; Kagan, C. R.; Fleischer, J. W.; Stone, H. A.; Loo, Y.-L. Wrinkles and Deep Folds as Photonic Structures in Photovoltaics. *Nat. Photonics* **2012**, *6*, 327−332.
(42) Meier, R.; Birkenstock, C.; Palumbiny, C. M.; Müller-Buschbaum, P. Efficiency-improved Organic Solar Cells Based on Plasticizer Assisted Soft Embossed PEDOT:PSS. *Phys. Chem. Chem. Phys.* **2012**, *14*, 15088−15098.
(43) Kaune, G.; Ruderer, M. A.; Metwalli, E.; Wang, W.; Couet, S.; Schlage, K.; Röhlsberger, R.; Müller-Buschbaum, P. In-situ GISAXS study of gold film growth on conducting polymer films. *ACS Appl. Mater. Interfaces* **2009**, *1*, 353−360.

(44) Roth, S. V.; Burghammer, M.; Riekel, C.; Müller-Buschbaum, P.; Diethert, A.; Panagiotou, P.; Walter, H. Self-assembled Gradient Nanoparticle-polymer Multilayers Investigated by an Advanced Characterisation Method: Microbeam Grazing Incidence X-ray Scattering. *Appl. Phys. Lett.* **2003**, *82*, 1935.
(45) Müller-Buschbaum, P.; Bauer, E.; Maurer, E.; Roth, S. V.; Gehrke, R.; Burghammer, M.; Riekel, C. Large-scale and Local-scale Structures in Polymer-blend Films: a Grazing-incidence Ultra-small-angle X-ray Scattering and Sub-microbeam Grazing-incidence Small-angle X-ray Scattering Investigation. *J. Appl. Crystallogr.* **2007**, *40*, S341−S345.
(46) Kesava, S. V.; Dhanker, R. D.; Kozub, D. R.; Vakhshouri, K.; Choi, U. H.; Colby, R. H.; Wang, C.; Hexemer, A.; Giebink, N. C.; Gomez, E. D. Mesoscopic Structural Length Scales in P3HT/PCBM Mixtures Remain Invariant for Various Processing Conditions. *Chem. Mater.* **2013**, *25*, 2812−2818.
(47) Hamilton, W. A. Conformation, Directed Self-assembly and Engineered Modification: Some Recent Near Surface Structure Determinations by Grazing Incidence Small Angle X-ray and Neutron Scattering. *Curr. Opin. Colloid Polym. Sci.* **2005**, *9*, 390−395.
(48) Renaud, G.; Lazzari, R.; Leroy, F. Probing Surface and Interface Morphology with Grazing Incidence Small Angle X-Ray Scattering. *Surf. Sci. Rep.* **2009**, *64*, 255−380.
(49) Müller-Buschbaum, P. Grazing Incidence Small-angle X-ray Scattering: an Advanced Scattering Technique for the Investigation of Nanostructured Polymer Films. *Anal. Bioanal. Chem.* **2003**, *376*, 3−10.
(50) Treat, N. D.; Brady, M. A.; Smith, G.; Toney, M. F.; Kramer, E. J.; Hawker, C. J.; Chabinyc, M. L. Interdiffusion of PCBM and P3HT Reveals Miscibility in a Photovoltaically Active Blend. *Adv. Energy. Mater.* **2011**, *1*, 82−89.
(51) Chen, W.; Xu, T.; He, F.; Wang, W.; Wang, C.; Strzalka, J.; Lin, Y.; Wen, J.; Miller, D. J.; Chen, J.; Hong, K.; Yu, L.; Darling, S. B. Hierarchical Nanomorphologies Promote Exciton Dissociation in Polymer/Fullerene Bulk Heterojunction Solar Cells. *Nano Lett.* **2011**, *11*, 3707−3713.
(52) Nikiforov, M. P.; Lai, B.; Chen, W.; Chen, S.; Schaller, R. D.; Strzalka, J.; Maser, J.; Darling, S. B. Detection and Role of Trace Impurities in High-performance Organic Solar Cells. *Energy Environ. Sci.* **2013**, *6*, 1513−1520.
(53) Kohn, P.; Rong, Z.; Scherer, K. H.; Sepe, A.; Sommer, M.; Müller-Buschbaum, P.; Friend, R. H.; Steiner, U.; Hüttner, S. Crystallization-Induced 10-nm Structure Formation in P3HT/PCBM Blends. *Macromolecules* **2013**, *46*, 4002−4013.
(54) Chou, K. W.; Yan, B.; Li, R.; Li, E. Q.; Zhao, K.; Anjoum, D. H.; Alvarez, S.; Gassaway, R.; Biocca, A.; Thoroddsen, S. T.; Hexemer, A.; Amassian, A. Spin-Cast Bulk Heterojunction Solar Cells: A Dynamical Investigation. *Adv. Mater.* **2013**, *25*, 1923−1929.
(55) Chou, K. W.; Khan, H. U.; Niazi, M. R.; Yan, B.; Li, R.; Payne, M. M.; Anthony, J. E.; Smilgies, D.-M.; Amassian, A. Late Stage Crystallization and Healing During Spin-coating Enhance Carrier Transport in Small-molecule Organic Semiconductors. *J. Mater. Chem. C* **2014**, *2*, 5681−5689.
(56) Chourou, S. T.; Sarje, A.; Li, X. S.; Chan, E. R.; Hexemer, A. HipGISAXS: a High-performance Computing Code for Simulating Grazing-incidence X-ray Scattering Data. *J. Appl. Crystallogr.* **2013**, *46*, 1781−1795.
(57) Salditt, T.; Metzger, T. H.; Peisl, J.; Reinker, B.; Moske, M.; Samwer, K. Determination of the Height-Height Correlation Function of Rough Surfaces from Diffuse X-Ray Scattering. *Europhys. Lett.* **1995**, *32*, 331−336.
(58) Müller-Buschbaum, P.; Perlich, J.; Abul Kashem, M. M.; Schulz, L.; Roth, S. V.; Cheng, J. Y.; Gutmann, J. S. Combinatorial Investigation of Nanostructures Formed in a Titanium Dioxide Based Nanocomposite Film on Top of Fluor-doped Tin Oxide Layers. *Phys. Status Solidi* **2007**, *1*, 119−121.